High resolution X-ray detector for synchrotron-based microtomography

Marco Stampanoni[a,b,*], Gunther Borchert[b,d], Peter Wyss[c], Rafael Abela[b], Bruce Patterson[b], Steven Hunt[b], Detlef Vermeulen[b], Peter Rüegsegger[a]

[a] *Institute for Biomedical Engineering, University of Zürich and ETHZ (IBT), Moussonstrasse 18, CH-8044 Zürich, Switzerland*
[b] *Swiss Light Source (SLS), Paul Scherrer Institute (PSI), Switzerland*
[c] *Swiss Federal Laboratories for Material Testing and Research (EMPA), Switzerland*
[d] *Institut für Kernphysik, Forschungszentrum Jülich, D-52425 Jülich, Germany*

Abstract

Synchrotron-based microtomographic devices are powerful, non-destructive, high-resolution research tools. Highly brilliant and coherent X-rays extend the traditional absorption imaging techniques and enable edge-enhanced and phase-sensitive measurements. At the Materials Science Beamline MS of the Swiss Light Source (SLS), the X-ray microtomographic device is now operative. A high performance detector based on a scintillating screen optically coupled to a CCD camera has been developed and tested. Different configurations are available, covering a field of view ranging from $715 \times 715\,\mu m^2$ to $7.15 \times 7.15\,mm^2$ with magnifications from $4\times$ to $40\times$. With the highest magnification 480 lp/mm had been achieved at 10% modulation transfer function which corresponds to a spatial resolution of $1.04\,\mu m$. A low-noise fast-readout CCD camera transfers 2048×2048 pixels within 100–250 ms at a dynamic range of 12–14 bit to the file server. A user-friendly graphical interface gives access to the main parameters needed for running a complete tomographic scan. This novel device will be used to study the physical structure and chemical composition of biological and technical materials, e.g. enabling pseudo-dynamic testing of bone samples to establish structure–function relationships in simulated osteoporosis or enabling non-destructive testing during the development of modern composite materials. © 2002 Elsevier Science B.V. All rights reserved.

*Corresponding author. Institute for Biomedical Engineering, University of Zürich and ETHZ (IBT), Moussonstrasse 18, CH-8044 Zürich, Switzerland. Tel.: +41-1-632-45-69; fax: +41-1-632-1214.
E-mail address: stampanoni@biomed.ee.ethz.ch (M. Stampanoni).

1. Introduction

X-ray computer microtomography is a well-known technique, which provides volumetric data of samples in a non-destructive way. Its application ranges from medicine to material sciences

[1–3]. Synchrotron radiation, as a highly brilliant X-ray source, pushes high-resolution examinations to the micrometer range. In addition, it extends the classical absorption tomography concepts towards edge-enhanced and phase-sensitive investigations. For these reasons, tremendous efforts are made all over the world to develop synchrotron-based microtomography devices (SRμCT) [4–7]. The most established detection method in SRμCT consists of converting X-rays into visible light with a scintillator and projecting them onto a CCD with the help of suitable microscopic optics. Different solutions have been proposed, and it has been shown that this type of detector reaches its limits when spatial resolution of one micrometer is approached [8]. In this paper the microtomographic device of the Swiss Light Source (SLS) is presented and its performance evaluated, with particular emphasis on the detector. In a first step, an instrument based on the standard detector method for the investigation of a wide spectrum of samples has been installed at the Materials Science Beamline MS of the SLS. This instrument measures objects at resolutions of the order of 1–5 μm. In a second step, a fully novel detector system, which will provide spatial resolution in the submicron range, will be incorporated.

The design goals of the SLS-instrument are fourfold: high spatial resolution, high efficient photon detection, fast-low-noise readout and high precision sample handling. This shall enable to combine dynamic mechanical tests with 3D-imaging in the micrometer range.

2. Materials and methods

2.1. Beamline layout

The Materials Science Beamline MS of the SLS is a multipurpose facility where X-ray microtomography, powder diffraction and in situ surface diffraction experiments will be carried out. The electron source size is 76 μm horizontally and 8 μm vertically (FWHM) and the beam divergence is $63.2 \times 3.0 \, \mu rad^2$. Synchrotron radiation is extracted at the straight section 4S of the SLS with a minigap hybrid wiggler with a period length of 61 mm. The angular acceptance in monochromatic mode (5–40 keV), determined by a fixed collimator in the front-end, is 0.23 mrad vertical by 2.5 mrad horizontal. A polychromatic "pink beam" mode, up to 32 keV, will also be available. Fig. 1A gives a
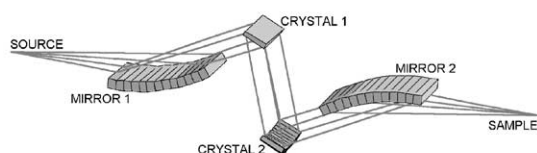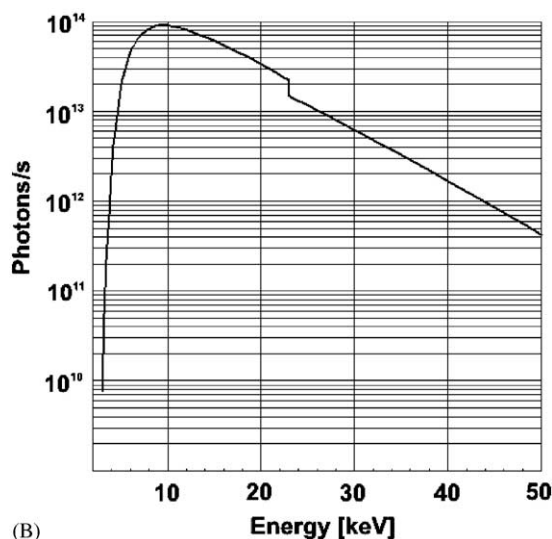

(A)   (B)

Fig. 1. (A) The optical system of the Materials Science Beamline MS: vertical collimating mirror (MIRROR 1), first monochromator flat crystal (CRYSTAL 1), second monochromator crystal for horizontal focusing (CRYSTAL 2) and vertical focusing mirror (MIRROR 2). (B) Expected monochromatic flux at the microtomography device for 400 mA ring current and wiggler gap of 7.5 mm.

schematic representation of the beam optics. Vertical collimation and focusing is provided by variable angle, variable curvature Rh-coated Si mirrors, which also serve to eliminate higher order harmonics. Monochromatization is performed by a fixed-exit double crystal Si (1 1 1) monochromator situated between the two mirrors delivering an inherent energy resolution of 0.014%. The second monochromator crystal can be bent to provide horizontal focusing. The optics produce a monochromatic flux density at 10 keV of $\approx 10^{14}$ photon/s which can be focused into a spot at the experimental stations of minimum size of $1\,mm^2$, see Fig. 1B. Thanks to the top-up injection mode, the intensity will be kept constant to a level of 10^{-3}–10^{-4} [9]. For the microtomography station, the source-to-sample distance is 35 m, resulting in a degree of coherence comparable with other synchrotron radiation sources [7].
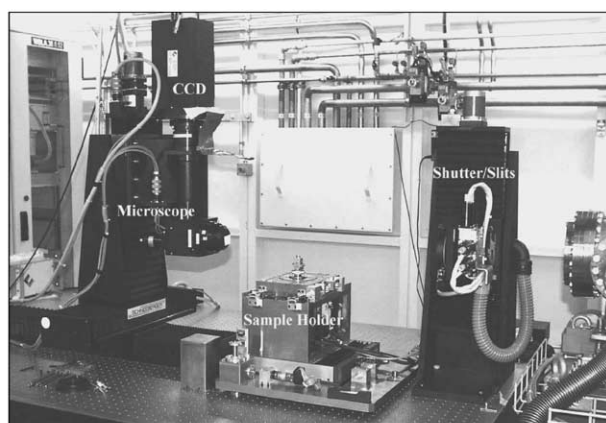
2.2. Microtomography device

The instrumentation is mounted on a Newport breadboard with enhanced vibration damping and steel honeycomb structure, see Fig. 2B. Synchrotron radiation can be tailored according to user requirements by four independent tungsten slits. In addition, an X-ray shutter can be used in order to reduce radiation damage on particular sensitive samples. The sample holder, manufactured by Kammrath&Weiss in Dortmund, allows the positioning of the specimen within a precision of $0.1\,\mu m$ as well as the correction of pitch, roll and yaw errors. Horizontal and vertical rotation axes will be available. The detector combines a transparent luminescent screen with a diffraction-limited microscope optic, which magnifies the sample projections onto a high-performance CCD camera (see Fig. 2B). Different Ce-doped $Y_3Al_5O_{12}$ (YAG) single crystal scintillator screens with thicknesses between 1.8 and $50\,\mu m$, deposited on a $190\,\mu m$ inactive YAG substrate are available for various efficiency needs and spatial resolution requirements. The YAG:Ce crystals have been manufactured by Crismatec Saint-Gobain, Nemours, France and their main physical and scintillation properties are summarized in Table 1. The microscope, manufactured by Optique Peter in Lyon, is equipped with a revolver, which can accommodate three different high-quality, diffraction-limited and aberration-corrected objectives allowing a quick change between different field of views and values of spatial resolution. The remote-controlled focusing mechanism matches the depths of focus of a broad variety of objectives. The focussing is done semi-automatically by maximization of the standard deviation of the mean pixel value of a portion of the image. The
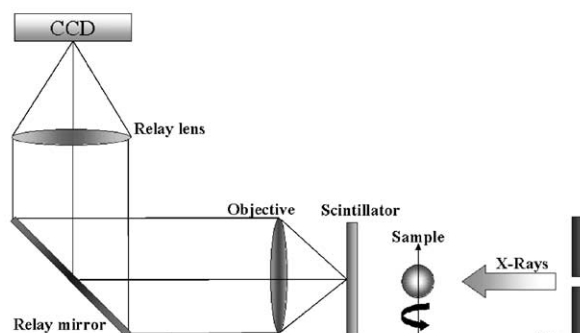
Fig. 2. (A) Schematic diagram of the detector system showing the geometry of irradiation. (B) Microtomography device at the beamline MS of the SLS. The synchrotron beam comes from the right: clearly visible are the shutter/slits assembly, the sample holder and the detector unit. The components are mounted on a Newport breadboard that can be precisely adjusted in the vertical direction.

CCD camera, manufactured by Pixel Vision of Oregon, Inc., is equipped with a Thomson Th7899M full-frame chip with 2048×2048 pixels of $14\,\mu m$ pitch. A full-frame can be read-out in 100–$250\,ms$ through four independent outputs at 12–14 bit dynamical range and data are stored directly to the SLS file server via a fiber optic link. The camera has an optical shutter (open–close cycle of 30–$40\,ms$) to reduce the afterglow effect of the scintillator and to allow a completely dark read-out. The entire detection system has a theoretical pixel size (pixel pitch divided by total magnification) of $0.35\,\mu m$ (when the $20 \times$ objective, with numerical aperture $NA = 0.7$ combined with the $2 \times$ relay lens is used) with a field of view of $715 \times 715\,\mu m^2$. If the $2 \times$ ($NA = 0.08$) objective is used, a field of view of $7.15 \times 7.15\,mm^2$ with theoretical pixel size of $3.5\,\mu m$ is guaranteed. The detector unit is mounted on a three-axis system from Schneeberger with a stroke along the beam direction of $1124\,mm$: this enables to increase the sample-detector distance to $1\,m$, making edge-enhanced imaging and holotomography possible.

2.3. Spatial resolution

Scintillating screens optically coupled to CCDs can be modeled as defocused systems as depicted in Fig. 3. X-rays create identical visible-light images in different planes of the scintillator and the final image is found by superimposing the intensity distributions originated in different objects planes. Image spatial resolution is determined by the amount of defect of focus of the image distributions before and behind the focal plane and, further, by diffraction and spherical aberration arising from the thickness of the scintillator and the substrate [8]. Hopkins investigated the physical properties of this system and we will apply his formulae to estimate the resolution of

Table 1
Main physical and scintillation properties of YAG:Ce

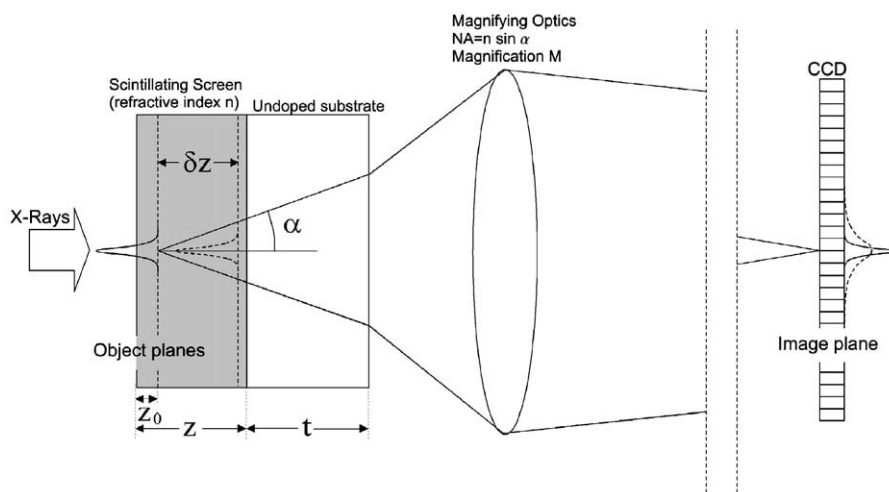| Physical properties	
Chemical formula	$Y_3Al_5O_{12}$
Crystal structure	Cubic
Density	$4.55\,g/cm^3$
Hygroscopic	No
Refractive index	1.95
Scintillating properties	
Integrated light output	40% NaI:Tl
Wavelength of max emission	550 nm
Conversion efficiency $\eta_{x/v}$	4%
Afterglow after 6 ms (50 ms)	<1% (0.1%)

Fig. 3. The X-ray beam creates identical visible-light images in different planes of the scintillator. An image in plane z_0 is focused onto the CCD. An image in plane $z_0 + \delta z$ is out of focus at the CCD, adapted from Ref. [8].

our detector. Considering a circular aperture, and neglecting any scattering effect inside the scintillator, the frequency response of the system can be described with [10]:

$$D(s) = \frac{4}{\pi a}\cos\left(\frac{1}{2}a|s|\right)\int_0^\beta \sin(a\cos\theta)\cos\theta\,\mathrm{d}\theta$$
$$- \frac{4}{\pi a}\sin\left(\frac{1}{2}a|s|\right)\int_0^\beta \cos(a\cos\theta)\cos\theta\,\mathrm{d}\theta \quad (1)$$

where s is the frequency variable and $a = (4\pi/\lambda)\,\omega_{20}|s|$ with λ being the wavelength of the light impinging on the system (for YAG:Ce, $\lambda = 550\,\mathrm{nm}$). The coefficient $\omega_{20} = \frac{1}{2}(NA^2/n)\,\delta z$ measures the focal shift, i.e. the optical path length between the reference sphere and the emergent wave front and n, NA and δz are the index of refraction, the numerical aperture and the amount of defect of focus, respectively. The geometrical significance of the limit $\beta = \cos^{-1}\left(\frac{1}{2}|s|\right)$ is described in Ref. [10]. The integrals in Eq. (1) can be evaluated using the expansion of the trigonometric contributions in terms of Bessel functions. The result is a combination of convergent series that are well suited for numerical simulation

$$D(s) =$$
$$\frac{4}{\pi a}\cos\left[\frac{a|s|}{2}\sum_{k=1}^{\infty}\frac{1}{2k}\sin(2k\beta(J_{2k-1}(a) - J_{2k+1}(a)))\right]$$
$$- \frac{4}{\pi a}\sin\left[\frac{a|s|}{2}\sum_{k=1}^{\infty}\frac{1}{2k}\sin(2k\beta(J_{2k-1}(a) - J_{2k+1}(a)))\right].$$
$$(2)$$

The optical transfer function (OTF) of the system is the sum of the individual frequency responses $D(s)$ and since the numerical aperture as well as the defect of focus can be considered as variables in Eq. (2) we can write

$$D(s) = D(f, \delta z, NA) \quad (3)$$

where $f = (NA/\lambda)\,s$ describes the frequency response of the system in the object plane. For z being the thickness of the scintillator, the OTF of the whole system can be expressed with

$$OTF(f, z, NA) = \int_{-z/2}^{z/2} D(f, \delta z, NA)\,\mathrm{d}\delta z. \quad (4)$$

Since the pupil function of the lens is symmetrical, the OTF is equal to the modulation transfer function (MTF) and we can finally write

$$MTF(f) = |OTF(f, z, NA)|$$
$$= \left|\int_{-z/2}^{z/2} D(f, \delta z, NA)\,\mathrm{d}\delta z\right|. \quad (5)$$

The MTF can be obtained experimentally from the Fourier transform of the measured line spread function (LSF) of the system. We recorded the LSF response of the detector by investigating its edge spread function (ESF). We used a $100\,\mu\mathrm{m}$ thick tantalum edge that was slightly rotated with respect to the CCD pixel columns for oversampling purposes. The quality of the sampled ESF has been improved by fitting the rebinned data to a linear superposition of three Fermi functions [11]. The non-linear regression has been performed with the Levenberg Marquardt's method provided by *Mathematica* [12]. The LSF has been obtained by analytical, noise-free derivation of the fitted ESF.

2.4. Quantum efficiency and noise

The detective quantum efficiency (DQE) is defined as the square signal-to-noise ratio (SNR) at the output relative to the SNR at the input of the detector. The noise of the input signal is given by $SNR_{in} = \sqrt{n_\gamma}$, according to Poisson statistics, where n_γ is the number of incident photons. The luminescent screen, lens coupled to a CCD camera is a cascaded detector system and its DQE is given by the sum of the variances of each single process [13]. Each process has a gain η_i, which is the ratio of outgoing quanta to incoming quanta. If $\eta_i \gg 1$, then the statistic of the process is given by the Poisson distribution, i.e. its variance is $v_i = 1/\eta_i$. If $\eta_i < 1$, then the process has a binomial statistics and $v_i = (1 - \eta_i)/\eta_i$. The whole detection process can be modeled with four different steps: X-ray absorption in the scintillator η_{abs}, energy-dependent fluorescence $\eta_{flu} = \eta_{x/v}E_x/E_v$, collection efficiency of the lens $\eta_{col} \approx (NA/2n)^2$ and quantum efficiency of the CCD $\eta_{v/e}$. Considering the detector response only at low spatial frequencies and in shot noise limited operation, the total DQE

of the system can be written as

$$DQE = \left(1 + \frac{1-\eta_{abs}}{\eta_{abs}} + \frac{1}{\eta_{abs}}\frac{1}{\eta_{flu}} + \frac{1}{\eta_{abs}\eta_{flu}}\frac{1-\eta_{col}}{\eta_{col}}\right.$$

$$\left. + \frac{1}{\eta_{abs}\eta_{flu}\eta_{col}}\frac{1-\eta_{v/e}}{\eta_{v/e}}\right)^{-1}. \tag{6}$$

The performance of the CCD in terms of noise and dynamic range has been investigated with the acquisition of photon transfer curves (PTC). The photon transfer technique has proven to be one of the most valuable CCD transfer curves for calibrating, characterizing and optimizing performance [14]. The PTC is the response of the CCD that is uniformly illuminated at different levels of light. Three distinct noise regimes can be identified in the curves: the read noise floor (random noise under totally dark conditions and ultimately limited by on-chip amplifiers and dark current), the shot noise (middle region of the curves) and the fixed-pattern noise associated with pixel non-uniformity noise. The system gain expressed in electrons per analog-digital numbers e^-/DN as well as the dynamical range can be obtained from these curves. The wavelength for the CCD illumination was 550 nm, the emission wavelength of YAG:Ce.

3. Results

3.1. Spatial resolution

We calculated the spatial resolution R of the detector by numerical simulation of Eq. (5) for different scintillator thicknesses and objectives (NA). The results, expressed in μm at 10% MTF are illustrated in Fig. 4. For low NA the optical system is limited by diffraction and the defect of focus (i.e. the scintillator thickness) does not affect the performance of the system. For high NA the curves split up depending on the amount of defect of focus. The data have been fitted with the function

$$R = \sqrt{\left(\frac{p}{NA}\right)^2 + (qzNA)^2}$$

with $\quad p = 0.34\,\mu m, q = 0.036 \tag{7}$

where the first term is due to diffraction and the second term to defect of focus. Our fitting parameters slightly deviate from other published values [8] because we choose the "10% MTF contrast" as figure of merit for the spatial resolution. Nevertheless, for a given resolution R, there is still a specific pair of parameters (z, NA), corresponding to a specific screen thickness and objective type, which minimizes R and therefore characterizes the best optical design. According to these theoretical results, we investigated three YAG:Ce scintillators with an active screen of 1.8, 20 and 51 μm thickness and inactive substrate of 190 μm. Fig. 5 compares the measured MTF responses of the detector for the three different screens when the $20\times$ objective was used. The theoretical pixel size was 0.35 μm and the field of view $715 \times 715\,\mu m^2$. For the 1.8 μm thick screen frequency responses up to 480 lp/mm at 10% MTF were detected, which correspond to a spatial resolution of 1.04 μm. For the 20 and 51 μm scintillator we recorded 350 and 210 lp/mm at 10% MTF, respectively. Optimal with regard to contrast and resolution was the 20 μm thick scintillator below 150 lp/mm. The 51 μm thick scintillator has the highest efficiency of all the tested screens and will be our first choice for rapid measurements. Its maximal resolution (280 lp/mm, i.e. 1.8 μm) is reached when the $10\times$ objective is used, according to the theory.

Fig. 6 represents the measured frequency response of the detector for different objectives when the 1.8 μm thick scintillator was used. The $20\times$ (NA = 0.7) objective showed the best contrast response. Objectives with smaller numerical aperture (NA = 0.46 for the $10\times$, NA = 0.16 for the $4\times$ and NA = 0.08 for the $2\times$) showed reduced frequency responses accordingly. At 10% MTF the resolution varies from 96 lp/mm (for the $2\times$) up to 480 lp/mm (for the $20\times$), which correspond to spatial resolutions between 5.2 and 1.04 μm. On the other hand, the $2\times$ objective provides a field of view 10 times larger than the $20\times$, which allows to investigate samples of about 7 mm diameter.

3.2. Quantum efficiency and noise

Table 2 summarizes the estimated DQE values at 10, 20 and 30 keV for a cascade system
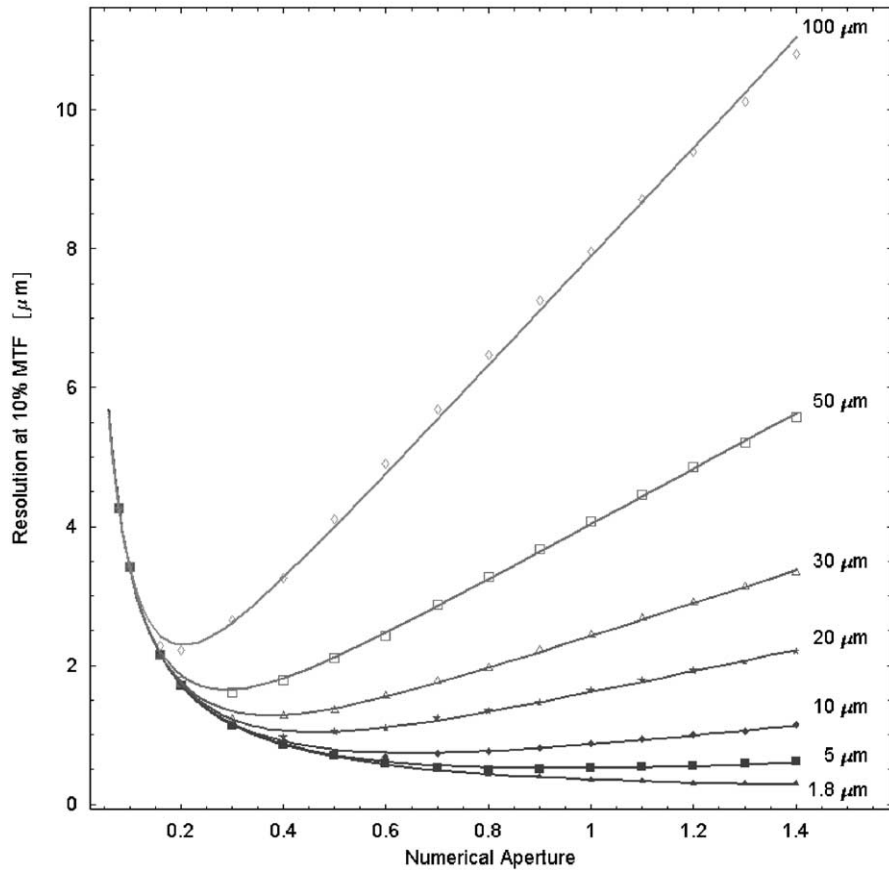
Fig. 4. Calculated spatial resolution R (expressed in μm at 10% MTF) vs. numerical aperture NA for an optical system with different scintillator thicknesses. According to Eq. (7) there is a pair (z, NA) for which the function R has a minimum. For example, for $z = 20\,\mu m$ the minimum lies at NA = 0.4.

consisting of a 5 μm YAG:Ce screen with a $20 \times$ objective (NA = 0.7) and a CCD quantum efficiency of 22%. The detector response is considered only at low spatial frequencies (because low MTF can also lower the DQE) and in shot noise limited operation. For energies ranging from 10 to 30 keV the DQE lies between 2% and 5% approximately. Note that YAG has its K-edge at 17.4 keV and that even if the absorption efficiency at 10 keV is higher than at 20 keV the DQE is smaller because the fluorescence process is more intense at 20 keV than at 10 keV.

We acquired photons transfer curves for two typical factory configurations of the CCD:

high-gain-high-bandwidth (HGHB) and low-gain-low-bandwidth (LGLB), see Fig. 7. Following Ref. [15], the system gain (e$^-$/DN), the noise floor (e$^-$) as well as the dynamic range (bits) of the CCD have been calculated. For the fast (full-frame read-out 100 ms) HGHB library we measured a system gain of 0.71 e$^-$/DN and a full-well of 42 ke$^-$. This corresponds to and a noise floor of 8 e$^-$ and a dynamic range of 12.28 bits. For the slow (full-frame read-out 250 ms) LGLB library we measured a gain of 2.86 e$^-$/DN and a full-well of 174 ke$^-$, which means a noise floor of 10 e$^-$ and a dynamic range of 14.06 bits.
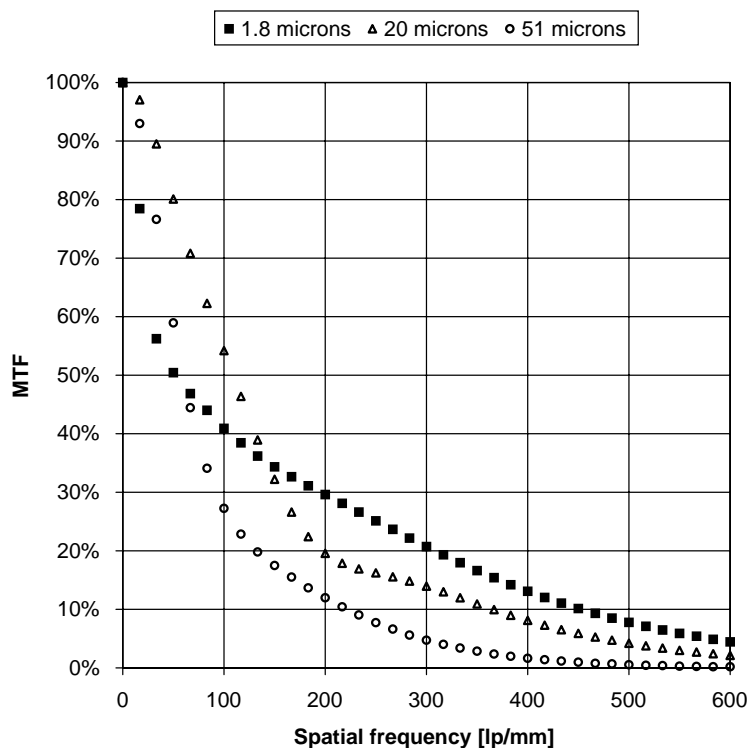
Fig. 5. Measured MTF response of the detector for 1.8, 20 and 51 μm thick YAG:Ce with the 20 × objective. Frequencies up to 480 lp/mm, corresponding to a spatial resolution of 1.04 μm at 10% MTF, have been recorded.

4. Discussion and outlook

In this work, the detector performance of the microtomography device at the SLS is described. Spatial resolutions ranging from 5 to 1 μm have been recorded for a field of view varying from 7 × 7 to 0.7 × 0.7 mm². Experimental results are in good agreement with theoretical predictions. One certain discrepancy between theory and experiment can be attributed to the contribution of the substrate, which was not included in the theory. This contribution can be relatively important especially for thin-doped layers and high X-ray energies (> 25 keV). The image quality is reduced since the depth of focus of the optics is too small to assure that the signal from the substrate is in focus [16]. For these reasons, the resolution measurements have been performed at 12 keV.

The low-noise CCD camera acquires frames of 2048 × 2048 pixels within 100–250 ms at dynamic ranges between 12 and 14 bits allowing time-resolved experiment with subsecond temporal resolution. The technical characteristics of our detector (chip-size, number of pixel, readout-speed and dynamic range) are the results of a series of compromises, which took into account the commercial availability of the CCD and cost. The detector, however, can easily be equipped with a larger CCD. Presently, objects up to 7 mm in diameter can be investigated with spatial resolution around 5 μm. Larger objects can be measured if local tomography is applied. Albeit it would be nice to measure large objects at ultrahigh resolutions, it should be kept in mind, that a 1 cm³ object measured at 1 μm resolution leads to a data set of 10^{12} voxels, still not very handy for routine work. At lower resolutions, such as 10 μm, table-top micro-CT devices are available [17] and SRμCT is not so badly needed as in the one micrometer range.
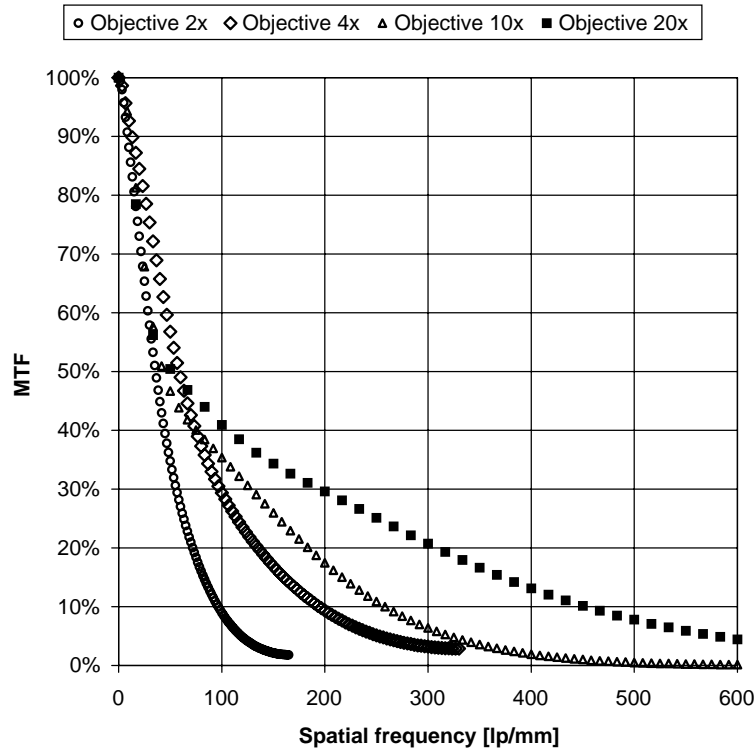
Fig. 6. Measured MTF response of the detector for different objectives with 1.8 μm thick YAG:Ce. Frequency responses from 96 lp/mm (5.2 μm) up to 480 lp/mm (1.04 μm) have been recorded. According to the theoretical predictions, the spatial resolution degrades when low-NA objectives are used.

Table 2
Estimated DQE of a cascade system at 10, 20 and 30 keV for 5 m YAG:Ce, NA = 0.7 and CCD quantum efficiency 22%

Process	η_i			v_i			DQE (%)		
Energies (keV):	10	20	30	10	20	30	10	20	30
Scint. abs., η_{abs}	0.08	0.07	0.02	11	13	40	8.44	7.00	2.45
Fluor. eff., η_{flu}	177	354	532	6×10^{-3}	3×10^{-3}	2×10^{-3}	8.40	6.98	2.44
Light coll., η_{col}		0.032			30.00		7.19	6.43	2.31
CCD QE, $\eta_{v/e}$		0.22			3.54		4.71	5.01	1.94

An additional aim of our SRμCT device is to exploit the usefulness of the coherent nature of the synchrotron. For a source size of 75.9 μm × 8 μm and a source-to-sample distance of 35 m the transversal coherence length is between 100 μm and 1 mm for energies between 5 and 40 keV. This property extends the classical absorption technique to edge-enhanced and phase-contrast imaging.

Two examples are given in Figs. 8 and 9 which show edge-enhanced radiographic projections of a housefly's head and a mosquito's knee acquired at 9 keV with our detector.

The SRμCT data are stored directly on the SLS file server and are immediately available for post-processing. Sinograms and several slices are reconstructed "on-line" for quality control
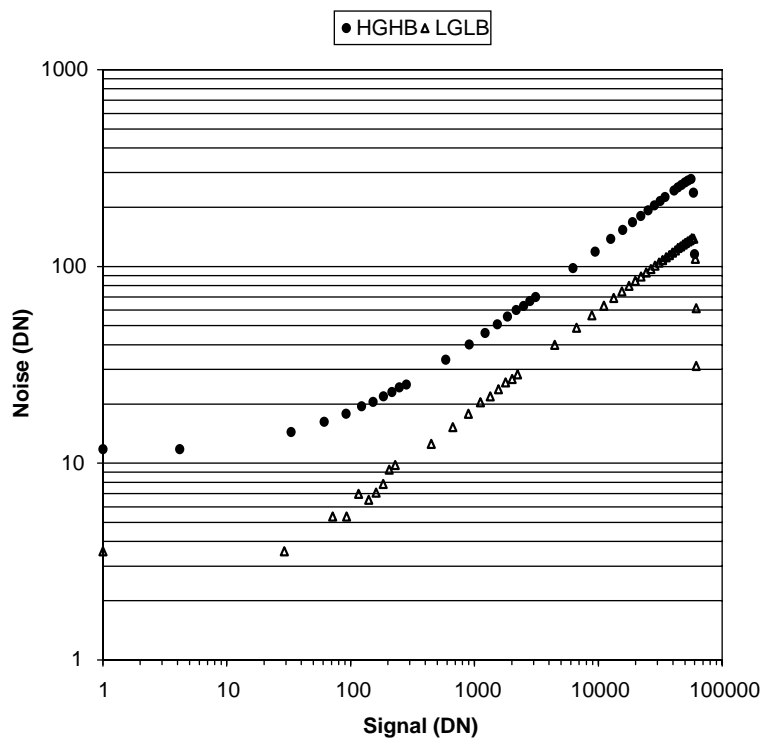
Fig. 7. Photon transfer curve for two different CCD configurations. The systems gain can be calculated from the slope of the curves in their linear range. The fast HGHB library showed a systems gain of $0.71\,e^-/DN$ and the slow LGLB library a gain of $2.86\,e^-/DN$. The readout noise was 8 and $10\,e^-$, respectively.
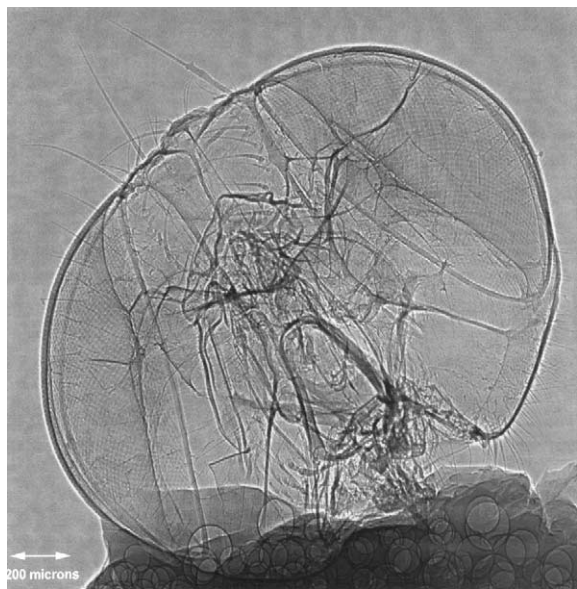

Fig. 8. Edge-enhanced radiographic projection of a housefly's head acquired at 9 keV. Sample-detector distance was 100 mm. Magnification was $8\times$, theoretical pixel size $1.75\,\mu m$.
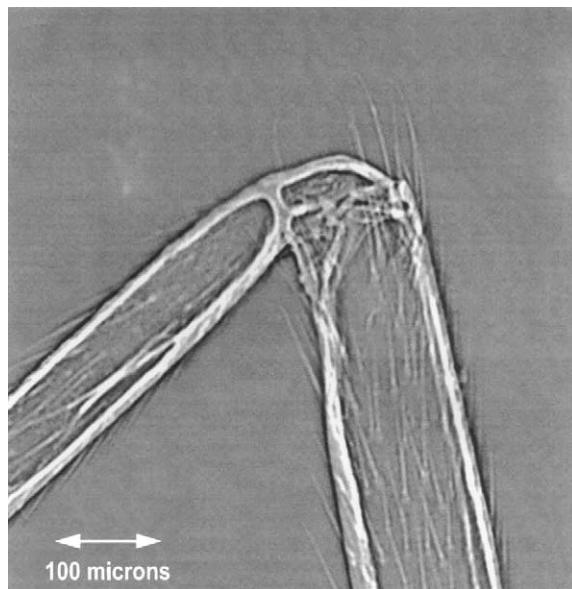

Fig. 9. Edge-enhanced radiographic projection of a mosquito's knee, acquired at 9 keV. Sample-detector distance was 100 mm. Magnification was $20\times$, theoretical pixel size $0.7\,\mu m$.

purposes. The full 3D reconstruction is performed offline. A Java graphical user interface (GUI) running on a standard Linux PC controls the microtomography device in a user-friendly way. The GUI panels easily access all the major features of the instrument: the user is able to choose energy, exposure time and acquisition mode with just a mouse-click. An expert mode allows the SLS crew to have full access to the instrument parameters for calibration and commissioning purposes. The communication with the CCD camera (which is controlled by an NT-based PC) is obtained with a Common Object Request Broker Architecture (CORBA) application based on the Mico 2.5 ORB [18] with IDL to C++ mapping and Java ORB 2.0 with IDL to Java mapping. CORBA allows complete transparent distributed computing reducing a complex CCD operation like read-out and direct in-memory addressing to a simple method's call.

In this work, it has been shown that the actual detector has almost reached its theoretical limits. This means that resolutions below 1 μm are hardly obtainable. From Fig. 4 it seems that just reducing the scintillator thickness and increasing the numerical aperture of the objectives could lead to submicron resolution. This is theoretically correct but practically hard to realize: first, it is difficult to work with wide-open objectives (NA > 1) since the field of view becomes very small and, second, reducing the thickness of the scintillator will lead to a very low efficiency. For these reasons, a second detector will be incorporated in the SRμCT device. The design goals of the new instrumentation are to *efficiently* trespass the micrometer barrier in terms of spatial resolution for hard X-ray (energies above 20 keV). The approach to achieve submicrometer resolution is to magnify the image with an X-ray optics and to detect it in low resolution, high efficiency mode, thus improving both resolution and efficiency. The novel detector has been extensively simulated and is expected to increase the efficiency of the standard detector by one order of magnitude without deterioring the spatial resolution [19].

References

[1] U. Bonse, F. Bush, O. Günnewig, F. Beckmann, R. Pahl, G. Delling, M. Hahn, W. Graeff, Bone Miner. 25 (1994) 5.

[2] U. Bonse, R. Nusshardt, F. Bush, R. Pahl, J.H. Kinney, Q.C. Johnson, R.A. Saroyan, M.C. Nichols, J. Mater. Sci. 26 (1991) 4076.

[3] B. Müller, P. Thurner, F. Beckmann, T. Weitkamp, C. Rao, R. Bernhardt, E. Karamuk, L. Eckert, J. Brandt, S. Buchloh, E. Wintermantel, D. Scharnweber, H. Worch, Non-destructive three-dimensional evaluation of biocompatible materials by microtomography using synchrotron radiation, Proceedings of the SPIE, Vol. 4503, 2002.

[4] U. Bonse, F. Bush, Prog. Biophys. Mol. Biol. 65 (1) (1996) 133.

[5] R. Lee, B. Lai, W. Yun, D. Mancini, Z. Cai, X-ray microtomography as a fast three-dimensional imaging technology using a CCD camera coupled with a CdWO4 single-crystal scintillator, Proceedings of the SPIE, Vol. 3149, 1997.

[6] B. Dowd, G.H. Campell, R.B. Marr, V. Nagarkar, S. Tipnis, L. Axe, D.P. Siddons, Developments in synchrotron X-ray computed microtomography at the National Synchrotron Light Source, Proceedings of the SPIE, Vol. 3772, 1999.

[7] T. Weitkamp, C. Raven, A. Snigirev. An imaging, microtomography facility at the ESRF beamline ID22, Proceedings of the SPIE, Vol. 3772, 1999.

[8] A. Koch, C. Raven, P. Spanne, A. Snigirev, J. Opt. Soc. Am. A 15 (7) (1998) 1940.

[9] B.D. Patterson, H. Auderset, F. Fauth, M. Lange P. Pattison, The materials science beamline, PSI Annual Report 1999, SLS Annex, p. 64.

[10] H.H. Hopkins, Proc. R. Soc. A 231 (1955) 91.

[11] A.P. Tzannes, J.M. Mooney, Opt. Eng. 34 (6) (1995) 1808.

[12] S. Wolfram, The Mathematica Book, 4th Edition, Wolfram Media/Cambridge University Press, Cambridge, 1999.

[13] C. Raven, Microimaging and Tomography with High Energy Coherent Synchrotron X-rays, Shaker Verlag, Aachen, 1998.

[14] J.R. Janesik, CCD characterization using the photon transfer technique, In K. Prettyjohns, E. Derenlak, (Eds.), Proceedings of the SPIE, Vol. 570, Solid State Imaging Arrays, 1985, pp. 7–19.

[15] J.R. Janesik, Scientific Charge-Coupled Devices, SPIE Press, Bellingham, WA, USA, 2001 (Chapter 2).

[16] A. Koch, P. Cloetens, W. Ludwig, J.C. Labiche, B. Ferrand, Reading thin-film scintillators with optical microscopes for X-ray imaging, Proceeding of the SCINT99, Moscow, 1999.

[17] P. Rüegsegger, B. Koller, R. Müller, Calcif. Tiss. Int. 58 (1996) 24.

[18] Mico Home Page, http://www.mico.org/, May 2001.

[19] M. Stampanoni, G.L. Borchert, R. Abela, B. Patterson, D. Vermeulen, P. Rüegsegger, P. Wyss, Acta Phys. Pol. B 33 (1) (2002) 463.